Chemical Engineering Journal 155 (2009) 534–541

Contents lists available at ScienceDirect

Chemical Engineering Journal

journal homepage: www.elsevier.com/locate/cej

Nanocrystalline zinc ferrite photocatalysts formed using the colloid mill and hydrothermal technique

Guoli Fan, Zhijun Gu, Lan Yang, Feng Li*

State Key Laboratory of Chemical Resource Engineering, P.O. Box 98, Beijing University of Chemical Technology, Beijing 100029, PR China

ARTICLE INFO

Article history:
Received 27 April 2009
Received in revised form 9 August 2009
Accepted 13 August 2009

Keywords:
Zinc ferrite
Nanostructure
Catalysis
Photo-degradation
Colloid mill
Synthesis

ABSTRACT

Nanocrystalline zinc ferrite ($ZnFe_2O_4$) photocatalysts with different crystallite sizes prepared using the colloid mill and hydrothermal technique are reported. This synthetic approach involves a very rapid mixing of Fe^{3+} cations with reducing agent and reduction process in a colloid mill reactor, followed by a slow oxidation of iron nuclei and structural transformation in a separate hydrothermal process. Material characterization has been presented by powder X-ray diffraction (XRD), chemical element analysis, X-ray photoelectron spectroscopy (XPS), scanning electron microscopy (SEM), energy dispersive X-ray spectroscopy (EDS), transmission electron microscopy (TEM) and UV–vis diffuse reflectance spectra. The results indicate that $ZnFe_2O_4$ nanocrystals with the uniform crystallite sizes have been obtained using *in situ* forming iron nuclei as the source of Fe. A possible formation mechanism of $ZnFe_2O_4$ nanocrystals was proposed. Furthermore, through photocatalytic investigation, these $ZnFe_2O_4$ nanocrystals displayed better abilities to photodecompose acid orange II azodye molecule under UV irradiation due to quantum confinement effect and high surface area structure, as compared to bulk $ZnFe_2O_4$ sample prepared by the conventional solid-state method. Since as-synthesized $ZnFe_2O_4$ nanocrystals have excellent chemical and thermal stabilities and exhibit good photocatalytic activities, it can be expected that they may have potential application in the field of industrial photo-degradation of organic azodye pollutants.

1. Introduction

In recent years, interest in transition metal ferrites of the type MFe_2O_4 nanocrystals has greatly increased due to their extensive use in high-density data storage, ferrofluid technology, magnetocaloric refrigeration, magnetic resonance imaging and heterogeneous catalysis [1–3]. For example, zinc ferrite ($ZnFe_2O_4$), known as semiconductor material, has a normal spinel structure with tetrahedral sites occupied by Zn^{2+} ions and octahedral sites by Fe^{3+} ions [4]. Its chemical and thermal stability has made $ZnFe_2O_4$ important materials, such as magnetic materials [5], catalysts [6–9], and absorbent materials [10,11], in the past decade. Particularly, increasing interests for nanoscale $ZnFe_2O_4$ have been extensively studied by worldwide researchers because of their unique size-dependent physical and chemical properties as compared to bulk counterpart materials [5].

It is well known that nanosized particles are of particular interest for catalytic applications due to their high surface to volume ratio. Several preparation techniques for $ZnFe_2O_4$ nanoparticles with uniform size have been developed including coprecipitation [11], sonochemical emulsification and evaporation [12], sol–gel technique [13], hydrothermal synthesis [14,15], mechanical milling [16,17], combustion method [18], reverse micelle technique [19], and organic precursor decomposition techniques [20–22]. However, in most of the above cases, they require handling of large amounts of organic salt, solvent or surfactant, which usually make expensive costs as well as environment pollution, and therefore are not suitable for large-scale industrial applications. On the other hand, it is generally accepted that the formation of homogeneous nanoparticles is strongly dependent on the local distribution of reactants or precursors, which is important for the nucleation and growth of nanoparticles. Therefore, it has always been a challenge or a hot issue to develop affordable and convenient synthesis route for nanoparticles with uniform crystallite size. Recently, we developed a facile pathway for the preparation of magnetic $CoFe_2O_4$ nanocrystals by a simple reduction–oxidation route [23]. This approach offers unique advantages for the uniform synthesis of special complex metal oxide nanoparticles due to the easily achievable high-speed nucleation of metallic precursors in the colloid mill reactor.

Semiconductor photocatalysts have been applied widely to degrade the organic pollutants for the remediation of hazardous wastes and contaminated groundwater, and the control of toxic air contaminants [24]. Much attention has been paid to the

* Corresponding author. Tel.: +86 10 64451226; fax: +86 10 64425385.
E-mail address: lifeng_70@163.com (F. Li).

1385-8947/$ – see front matter © 2009 Elsevier B.V. All rights reserved.
doi:10.1016/j.cej.2009.08.008

photocatalytic degradation of dyes with semiconductor compounds especially like TiO_2 under UV-light. In this contribution, we carefully investigate the uniform synthesis, microstructure and UV-light induced photo-degradation performance of nanocrystalline $ZnFe_2O_4$ with a narrow range of crystallite size. $ZnFe_2O_4$ nanocrystals were prepared via a modified reduction–oxidation route on the basis of the idea that slow oxidation of iron nuclei formed during the reduction in the colloid mill reactor has a remarkable inhibition effect on the growth of $ZnFe_2O_4$ under the hydrothermal conditions. To the best of our knowledge, there is no report on *in situ* forming iron nuclei precursor as the source of Fe for $ZnFe_2O_4$ nanocrystals. This applied approach, which needs neither the decomposition of complicated organic–metal complex precursors nor a large amount of specialized surfactants as template, is of significant importance in industrial applications as a consequence of low costs, benignancy to environment and synthetic convenience. Furthermore, the photocatalytic results show that resultant nanostructured $ZnFe_2O_4$ displayed better abilities to photodecompose acid orange II azodye molecule under UV irradiation due to quantum confinement effect and high surface area structure, as compared to bulk $ZnFe_2O_4$ sample prepared by the conventional solid-state method. It can be expected that as-synthesized zinc ferrite nanocrystals may have potential application in the field of industrial photo-degradation of organic azodye pollutants due to their excellent structural properties, such as thermal stability and strong resistance to acid and alkali.

2. Experimental

2.1. Synthesis of $ZnFe_2O_4$ nanocrystals

In a typical synthesis, three separate solutions were prepared prior to the synthesis. Solution A: analytical-grade $Fe(NO_3)_3{\cdot}9H_2O$ were dissolved in 50 mL of deionized water. Different concentrations of Fe^{3+} ions (0.088, 0.26 and 0.44 M) were used. Solution B: sodium borohydride was dissolved in 25 mL of deionized water to form a solution with the $[NaBH_4]/[Fe^{3+}]$ molar ratio of 2.0. Solution C: analytical-grade $Zn(NO_3)_2{\cdot}6H_2O$ were dissolved in 25 mL of deionized water to give a solution ($[Zn^{2+}] = 1/2[Fe^{3+}]$). Solutions A and B were simultaneously added rapidly to a colloid mill with rotor speed set at around 6000 rpm and mixed for 2 min, and then the resulting slurry was mixed with solution C. The mixture slurry was sealed in a Teflon-lined autoclave and heated at 120 °C for 12 h, respectively. The suspension was washed with deionized water several times and then ethanol, separately, and the obtained solid was dried at 80 °C for 12 h.

2.2. Characterization

Powder X-ray diffraction (XRD) patterns of the samples were collected using a Shimadzu XRD-6000 diffractometer under the following conditions: 40 kV, 30 mA, graphite-filtered Cu Kα radiation ($\lambda = 0.15418$ nm). The samples, as unoriented powders, were step-scanned in steps of 0.04° (2θ) using a count time of 10 s/step.

Elemental analysis for metal ions in samples was performed using a Shimadzu ICPS-75000 inductively coupled plasma emission spectrometer (ICP-ES). Samples were dried at 100 °C for 24 h prior to analysis, and solutions were prepared by dissolving the samples in dilute hydrochloric acid (1:1) for 24 h at room temperature.

Room temperature Fourier transform infrared (FT-IR) spectra were recorded in the range 4000–400 cm^{-1} with 2 cm^{-1} resolution on a Bruker Vector-22 Fourier transform spectrometer using the KBr pellet technique (1 mg of sample in 100 mg of KBr).

X-ray photoelectron spectra (XPS) was recorded on a Thermo VG ESCALAB250 X-ray photoelectron spectrometer at a pressure of about 2×10^{-9} Pa using Al Kα X-ray as the excitation source. The binding energy (BE) calibration of the spectra has been referred to carbon 1s peak, located at BE = 284.8 eV.

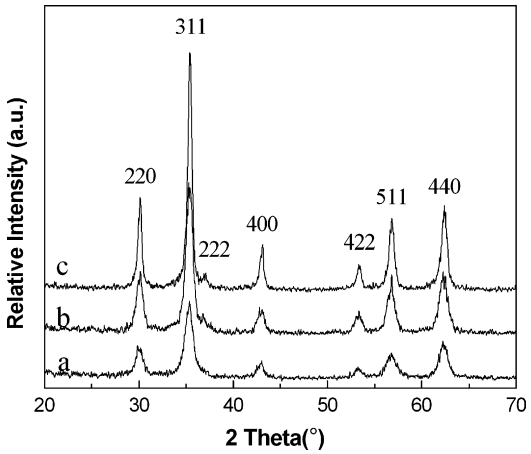

Fig. 1. XRD patterns for $ZnFe_2O_4$ synthesized by using different initial Fe^{3+} concentrations (a) 0.088 M, (b) 0.26 M and (c) 0.44 M.

Scanning electron microscopy (SEM) microanalyses of the samples were made using a Hitachi S4700 apparatus with the applied voltage of 20 kV, combined with energy dispersive X-ray spectroscopy (EDS) for the determination of metal composition.

Transmission electron microscopy (TEM) images were taken using a Hitachi H-800 transmission electron microscopy operated at 100 kV. For TEM analysis, a droplet of the ultrasonically dispersed samples in ethanol was placed onto an amorphous carbon-coated copper grid and then dried at air. High resolution transmission electron microscopy (HRTEM) was carried on a JEM-3010 high resolution transmission electron microscopy at an accelerating voltage of 200 kV.

The specific surface area determination was performed by BET method using a Quantachrome Autosorb-1C-VP Analyzer.

Solid state UV–vis diffuse reflectance spectra (DRS) were recorded at room temperature and in air by means of a Shimadzu UV-2501PC spectrometer equipped with an integrating sphere attachment using $BaSO_4$ as background.

2.3. Photo-degradation experiments

The photo-degradation experiments for acid orange II (AO-II) dye molecule over $ZnFe_2O_4$ ferrites were performed in a quartz reactor at ambient temperature. The UV source was two 36 W of H-type lamps (Beijing electric light sources research institute) with a maximum emission at approximately 254 nm. Typically, an aqueous AO-II solution (20 mg/L, 100 mL) containing 0.05 g of catalyst was vigorously stirred for 0.5 h in the dark to reach absorption–desorption equilibrium before the irradiation. Then, the mixture solution was irradiated by UV-light for a period of time. The extent of dye decomposition was determined by measuring the absorbance value at approximately 484 nm using a Shimadzu UV-2501PC spectrometer.

3. Results and discussion

3.1. Synthesis of $ZnFe_2O_4$ ferrite nanocrystals

Fig. 1 displays the powder XRD patterns for three $ZnFe_2O_4$ samples obtained by using different initial concentrations of Fe^{3+} ions. The high background of the profiles arises due to fluorescence from the Fe atoms [25]. All diffraction peaks can be indexed in a simple cubic lattice and the position along with relative intensity of

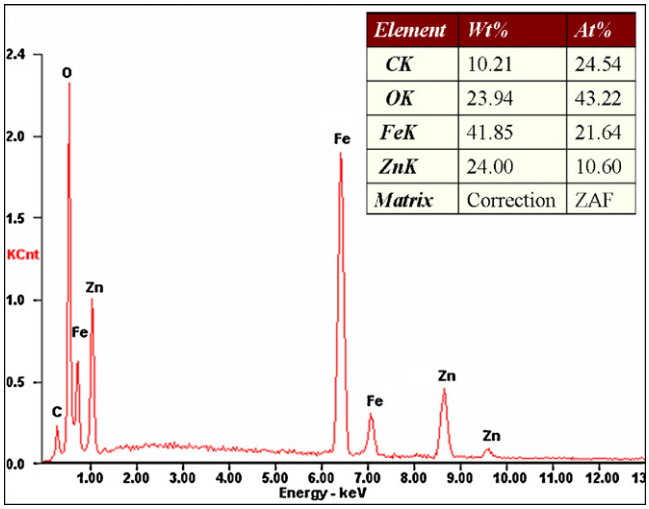

Fig. 2. EDS of $ZnFe_2O_4$ sample synthesized by using initial Fe^{3+} concentration of 0.088 M.

peaks match well with standard $ZnFe_2O_4$ powder diffraction data (JCPDS 89-4926), which indicates the obtained products have a *Fd*3*m* cubic spinel structure and are of high purity. According to the cubic crystal structure of spinel phase, the values of lattice parameter *a* determined from the most intense (3 1 1) reflection of XRD patterns using the formula $(1/d_{hkl}^2 = (h^2 + k^2 + l^2)/a^2$, *h k l* = 3 1 1) are 0.8441, 0.8439 and 0.8436 nm, respectively, with the increase in concentrations of initial Fe^{3+} ions, well consistent with that of bulk $ZnFe_2O_4$ (0.8443 nm). Elemental analysis by ICP-ES gives Zn/Fe atomic ratio of 0.48–0.51 in three samples, indicating that these samples are indeed zinc ferrite with the chemical formula of $ZnFe_2O_4$. In addition, EDS analysis (Fig. 2) shows that the sample using initial Fe^{3+} concentration of 0.088 M is composed of Zn, Fe and O elements, and the atomic ratio of Zn/Fe/O obtained is very close to 1/2/4 with the expected stoichiometric proportion for $ZnFe_2O_4$. Also, the presence of C signal within the spectrum arises from external contaminator. The aforementioned results confirm the formation of pure $ZnFe_2O_4$ phase.

On the other hand, the average crystallite size (coherent diffraction domain size) of $ZnFe_2O_4$ samples may be estimated from the values of full-width at half-maximum (FWHM) of the (3 1 1), (4 0 0) and (4 4 0) diffraction peaks by means of the Scherrer equation [$L = 0.89\lambda/\beta(\theta)\cos\theta$] [26], where L is the crystallite size, λ is the wavelength of the radiation used (0.15418 nm), θ is the Bragg diffraction angle, and $\beta(\theta)$ is the full-width at half-maximum (FWHM) of the (3 1 1), (4 0 0), and (4 4 0) reflections. FWHM is modified for instrumental broadening by the formula $B = B(M) - B^2(S)/B(M)$ [27], where $B(M)$ is FWHM of a given reflection for the prepared sample and $B(S)$ is that of a reflection taken for a standard SiC sample with a known average crystallite size larger than 10 μm. With the increase of the initial metal concentration, the estimated average crystallite size for the $ZnFe_2O_4$ samples is about 9.0, 14.0 and 19.0 nm, respectively.

The morphological characteristics of the obtained $ZnFe_2O_4$ were investigated by SEM and TEM analysis. SEM photographs of $ZnFe_2O_4$ samples (Fig. 3) reveal that all samples exhibit a compact arrangement of homogeneous nanoparticles with roughly spherical shape. TEM micrographs (Fig. 4) also confirm the nature of uniform particle size. Indeed, each sample is formed by particles, the average crystallite sizes (from the counting of about 100 particles) of $ZnFe_2O_4$ nanoparticles are 9 ± 3, 15 ± 6 and 22 ± 5 nm, respectively. Since the average crystallite size estimated from TEM micrographs and the coherent diffraction domain size inferred from XRD results are in good agreement, one could say that $ZnFe_2O_4$ nanoparticles are monodisperse nanocrystals. The HRTEM and selected area electron diffraction (SAED) analysis (Fig. 5) also provides more detailed structural information about the $ZnFe_2O_4$ ferrite. A typical HRTEM image of an individual $ZnFe_2O_4$ nanocrystal indicates interplanar distance of 0.299 nm that are characteristic of (2 2 0) spinel planes. Moreover, the SAED pattern taken from several individual 9 nm $ZnFe_2O_4$ nanocrystals reveals that the positions of discernible diffraction rings match well with standard $ZnFe_2O_4$ powder diffraction data. The above results support the nanocrystalline and monodisperse nature of as-synthesized $ZnFe_2O_4$ samples.

Unlike ZnO/Fe_2O_3 precursors used as the source of Zn and Fe employed for the synthesis of $ZnFe_2O_4$ in the solid-state reactions, Zn^{2+}/Fe precursors were alternatively employed in the present sys-

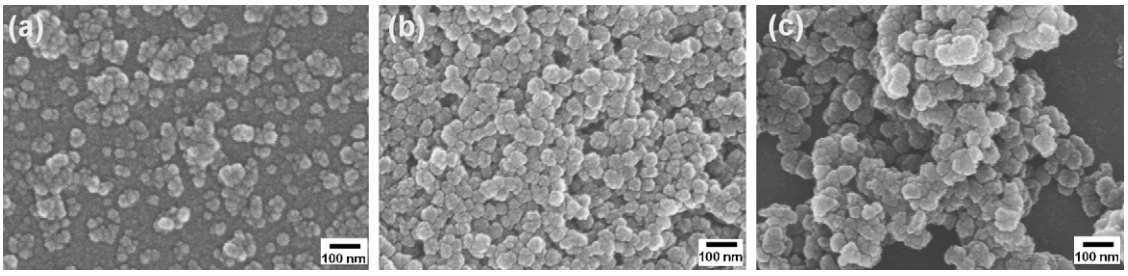

Fig. 3. SEM images for $ZnFe_2O_4$ samples with different crystallite sizes of (a) 9 nm, (b) 14 nm and (c) 19 nm.

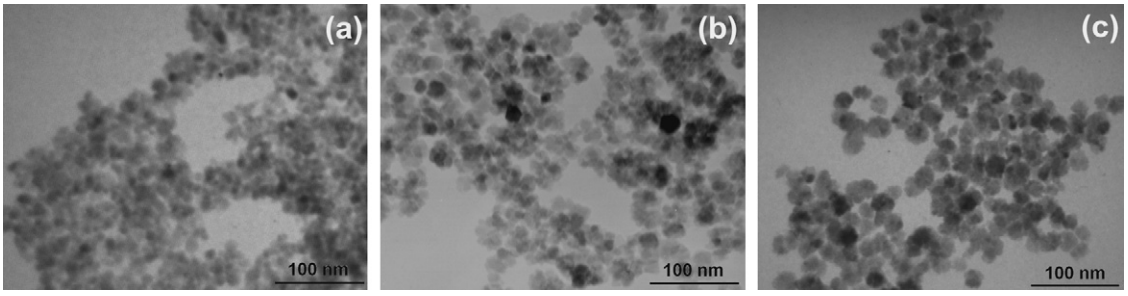

Fig. 4. TEM images for $ZnFe_2O_4$ samples with different crystallite sizes of (a) 9 nm, (b) 14 nm and (c) 19 nm.

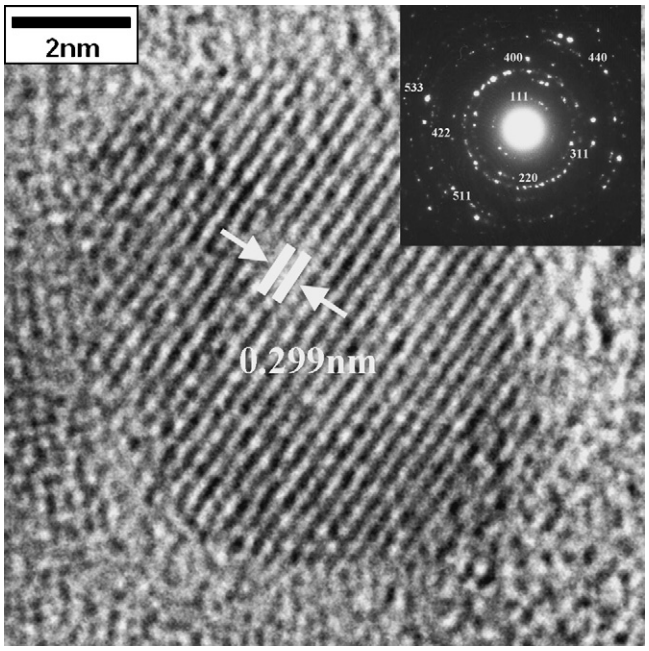

Fig. 5. HRTEM image of 9 nm $ZnFe_2O_4$ sample. The inset pattern is the electron diffraction pattern.

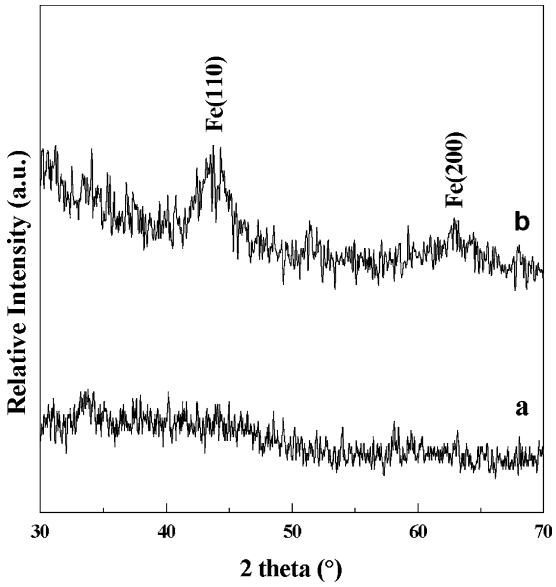

Fig. 6. XRD patterns for reduced immediate products in the colloid mill (a) without aging and (b) aging for 3 h at room temperature under N_2 atmosphere.

tem. Herein, the mixing of Fe^{3+} cations with reducing agent and nucleation of metallic iron are completed within a very short time in the vigorously stirring colloid mill reactor, and thus the process that nucleation of iron and nuclei growth take place simultaneously can be avoided, which facilitates to obtain nuclei with a narrow range of crystallite sizes [28]. In order to understand the mechanism of synthesis, XRD analysis for the reduced intermediate product collected from the colloid mill was carried out. XRD pattern only reveals the presence of amorphous phase (Fig. 6a). Moreover, after the reduced intermediate product is further aged for 3 h at room temperature under N_2 atmosphere, XRD pattern of resulting sample exhibits weak characteristic (1 1 0) and (2 0 0) reflections of body-centered cubic (bcc) α-Fe (Fig. 6b), consistent with the reported data (JCPDS 06-0696). The aforementioned results further indicate that iron nuclei can form through rapid reduction of $NaBH_4$ in the colloid mill.

On the other hand, the reduction takes place in a thin liquid film under conditions of high-speed fluid shear and high pressures and friction between the stator and rotor (rotating at 6000 rpm) with the mixture also being subjected to intensive vibration. In this highly turbulent zone, the newly formed metallic iron nuclei undergo energetic collisions and this, together with the strong hydraulic shear forces to which the nucleation mixture is subjected, means that agglomeration of the nuclei of iron is inhibited and their sizes remain at a minimum. As a result, the mechanism of $ZnFe_2O_4$ ferrite formation is proposed as follows (Eqs. (1)–(3)):

$$4Fe^{3+} + 3BH_4^- + 12H_2O \rightarrow 4Fe + 3B(OH)_4^- + 6H_2 + 12H^+ \quad (1)$$

$$4Fe + 3O_2 + 6H_2O \rightarrow 4Fe(OH)_3 \quad (2)$$

$$2Fe(OH)_3 + Zn^{2+} \rightarrow ZnFe_2O_4 + 2H_2O + 2H^+ \quad (3)$$

The formation mechanism for $ZnFe_2O_4$ nanocrystals is proposed and illustrated schematically in Fig. 7. In the initial step, the Fe^{3+} cations were rapidly reduced to metallic iron nuclei in the colloid mill (Eq. (1)), using $NaBH_4$ as reducing agent [29]. Then, the formed metallic iron nuclei reacted through a slow oxidation with the residual trace amount of dissolved oxygen and transform into corresponding $Fe(OH)_3$ compounds under the hydrothermal conditions (Eq. (2)). At last, the newly formed $Fe(OH)_3$ diffused into the Zn^{2+}-containing solution and reacted with Zn^{2+} ions, through a dehydration reaction under hydrothermal conditions [30], thus giving rise to $ZnFe_2O_4$ nanocrystals with the uniform crystallite sizes (Eq. (3)). Here, slow oxidation of iron nuclei exhibits a remarkable inhibition effect on the growth of $ZnFe_2O_4$. Additionally, in this method, the larger concentration of Fe^{3+} cations could favor the growth of larger ferrite nanocrystals. It is because the increase in the metal concentration could lead to the formation of a larger amount of metallic iron nuclei in the colloid mill reactor. Consequently, during the hydrothermal process, due to the limited trace amount of dissolved oxygen, the nucleation rate of ferrite nuclei, which are formed through the slow oxidation of metal nuclei followed by the diffusion of $Fe(OH)_3$, is almost same for each sample. At last, the

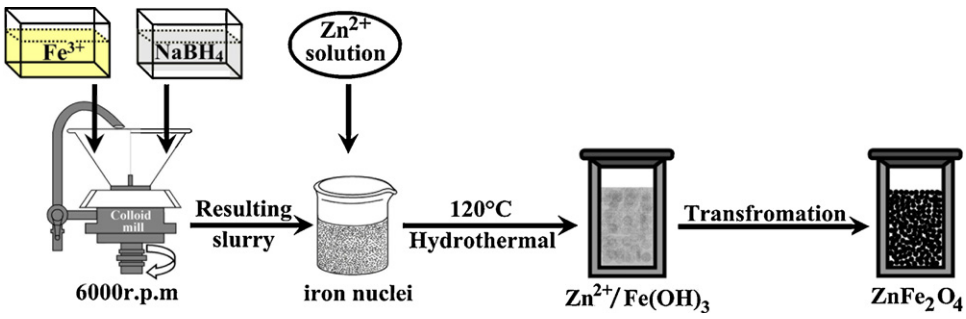

Fig. 7. Schematic illustration of the synthesis of $ZnFe_2O_4$ nanocrystals.

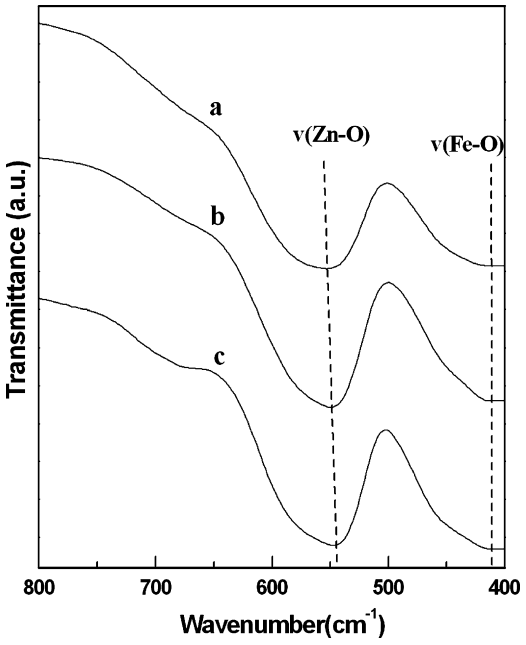

Fig. 8. FT-IR spectra for $ZnFe_2O_4$ samples with different crystallite sizes of (a) 9 nm, (b) 14 nm, (c) 19 nm.

dissolution of a larger amount of iron nuclei is advantageous to the growth of ferrite crystallites, thus leading to the formation of $ZnFe_2O_4$ ferrite with larger crystallite size.

3.2. Structural properties of $ZnFe_2O_4$ nanocrystals

The presence of the spinel structure for $ZnFe_2O_4$ samples is further confirmed by FT-IR spectroscopy (Fig. 8). There are two strong characteristic absorption peaks at about 550 and 415 cm^{-1}, which can be assigned to the stretching vibrations of the Zn–O bonds in tetrahedral positions and the Fe–O bonds in octahedral positions, respectively [31]. In addition, it is noteworthy that with the increase of crystallite size, a slight shift for the stretching vibration of the Zn–O bonds from 553 to 542 cm^{-1} can be observed. It is well documented that the decrease in crystallite size of $ZnFe_2O_4$ nanoparticles favors the redistribution of Zn^{2+} cations to octahedral sites in spinel structure [32], in spite of the high affinity of Zn^{2+} ions in tetrahedral sites. In addition, it is well known that the tetrahedrally coordinated Zn–O distance is shorter than octahedrally coordinated Zn–O distance in cubic spinel structure. Therefore, with the decreasing crystallite size of $ZnFe_2O_4$ nanoparticles, the number of octahedrally coordinated Zn–O bonds increase gradually, thus leading to the observed shift of Zn–O vibration in IR spectra. On the other hand, in view of crystalline electric field effect and size effect, the crystals with smaller crystallite size have more intensive distortion of lattices and higher strength of surface chemical bonds [33], also leading to the change in IR spectra to some extent.

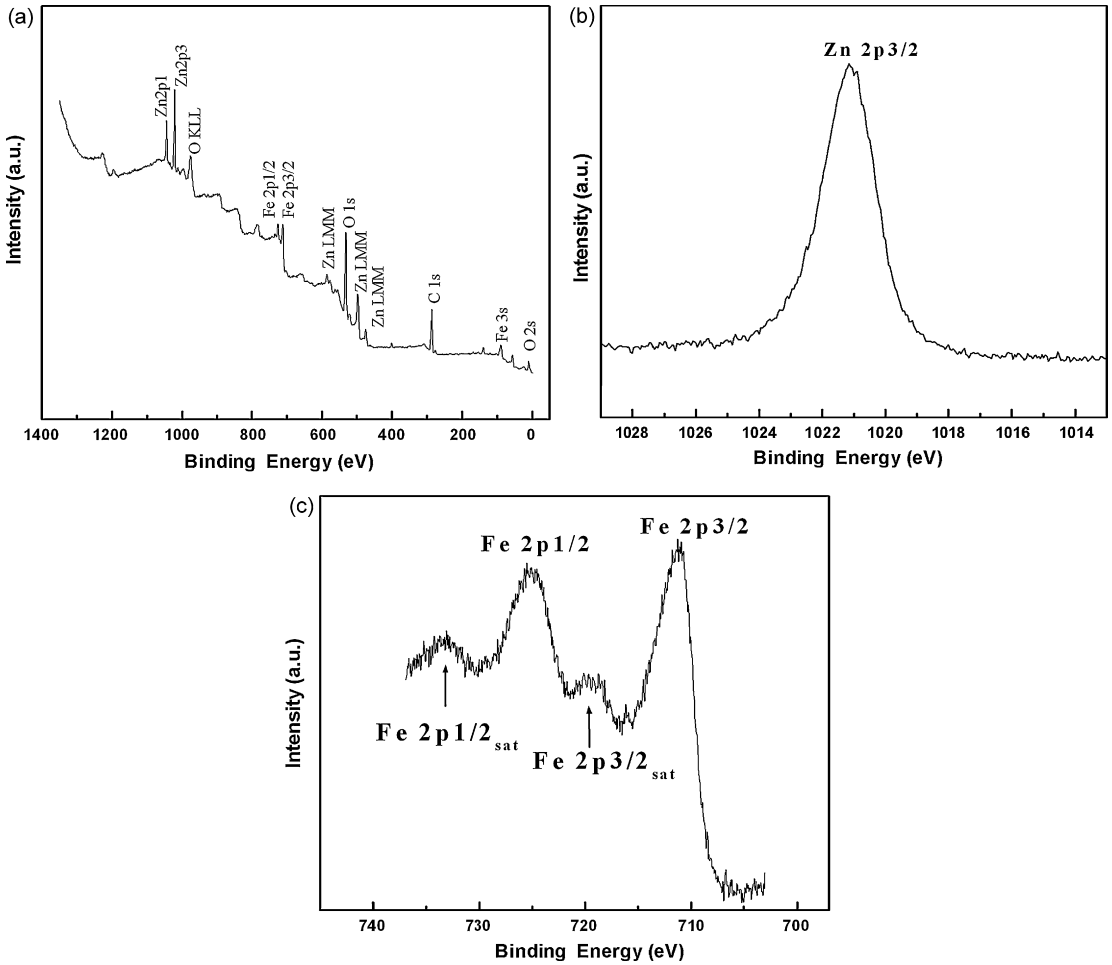

Fig. 9. XPS spectra of 9 nm $ZnFe_2O_4$ sample: (a) survey (b) Zn 2p and (c) Fe 2p.

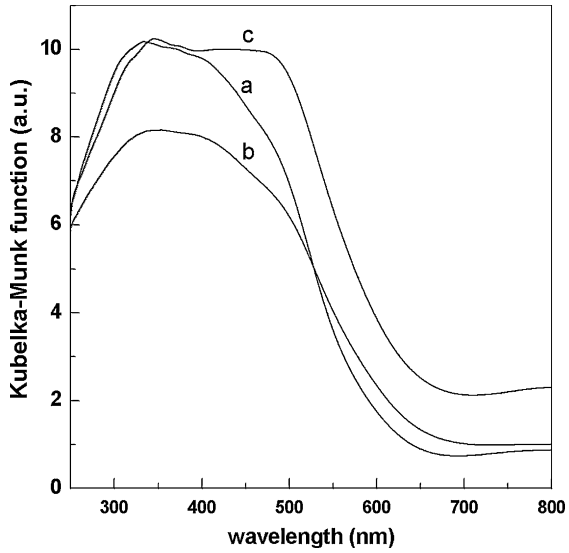

Fig. 10. UV–vis diffuse reflectance spectra of $ZnFe_2O_4$ with different crystallite sizes of (a) 9 nm, (b) 14 nm and (c) 19 nm.

The surface/near-surface chemical states of the obtained 9 nm $ZnFe_2O_4$ sample are analyzed by XPS within a range of binding energies of 0–1200 eV (Fig. 9a). Core levels of Zn 2p and Fe 2p can be identified, and no contaminant species are detectable within the sensitivity of the technique. Only a very low peak from absorbed carbon is present on the spectra. The fine spectra of the Zn 2p and Fe 2p peaks are displayed in Figs. 9b and c, respectively. The binding energy of the Zn 2p3/2 peak is 1021.1 eV, indicative of the presence of Zn^{2+} species. The Fe 2p3/2 and Fe 2p1/2 spectrum obtained from the present study generally shows two distinguishable main peaks at BE of around 711.0 and 724.9 eV, respectively, accompanied by two corresponding satellite peaks for Fe 2p3/2 and Fe 2p1/2 visible at BE of around 718.9 and 733.0 eV, only indicative of the presence of Fe^{3+} cations [34,35].

Generally, the chemical states of the species characterized by means of an ordinary XPS route only should be considered representative of the surface or external layers composition of the synthesized ferrite samples. However, by integrating the core-level intensities, the obtained Zn/Fe atomic ratio is 0.52, very close to that obtained by ICP and EDS analysis. This further reflects the homogeneous nature of as-synthesized $ZnFe_2O_4$ nanocrystals.

To give important information concerning the effect of crystallite size on the optical properties of $ZnFe_2O_4$ semiconductor materials, the UV–vis diffuse reflectance measurement was carried out (Fig. 10). The optical absorbance can be approximately calculated from the optical reflectance data by the Kubelka–Munk function, $\alpha = (1-R)^2/2R$, where α is the absorption coefficient, R is the diffuse reflectance [36]. As shown in Fig. 10, the as-synthesized $ZnFe_2O_4$ nanocrystals are highly photoresponsive in both the UV and visible light ranges (>400 nm) as expected. Especially, in the wavelength range of 300–500 nm, three samples present the strong light absorbance (in term of Kubelka–Munk equivalent absorbance units), indicative of wider absorption band than TiO_2.

It is well known that when semiconductors are irradiated by photons with energy similar to the band gap, they can yield an electron (e−) in the conduction band and a hole (h+) in the valence band. For a large number of semiconductors, the dependence of the absorption coefficient α, for the high-frequency region, upon the photon energy E_p, for optically induced transitions, is usually given by the following expression [37]:

$$\alpha E_p = K(E_p - E_g)^n \quad (4)$$

where E_g represents the optical band gap, E_p is the photon energy, K is a constant, and n depends on the nature of the transition. In fact, n assumes a value of 1/2, 3/2, 2, and 3 for allowed direct, forbidden direct, allowed indirect, forbidden indirect transitions, respectively. By analysis of absorption coefficients for $ZnFe_2O_4$, the optical energy gaps can be estimated using a classical Tauc approach [38]. As for three $ZnFe_2O_4$ nanocrystal samples, the best fit of $(\alpha E_p)^2$ vs E_p was obtained for $n = 1/2$ (Fig. 11), suggesting the allowed direct transitions across the energy band gap of $ZnFe_2O_4$. The extrapolated value (the straight lines to the x axis) of E_p at $\alpha = 0$ gives absorption edge energies corresponding to energy band gap (E_g) of 2.10 for 9 nm $ZnFe_2O_4$ sample, 2.00 for 14 nm sample and 1.92 eV for 19 nm sample, respectively. The noteworthy feature is a direct relationship between the grain size of the nanoparticles and optical band gap. The shift in E_g of the $ZnFe_2O_4$ nanoparticles with the increasing crystallite sizes is the result of quantum confinement effects arising from the small size regime [38,39].

3.3. Photo-degradation properties of $ZnFe_2O_4$ nanocrystals

As discussed above, as-synthesized $ZnFe_2O_4$ nanocrystal is a semiconductor with the optical adsorption threshold in the range of 590–645 nm. Photocatalytic process is based on the generation of electron/hole pairs by means of band-gap radiation, which can give rise to redox reactions with species adsorbed on the surface of the catalysts. In addition, the BET analysis shows that the specific surface areas of $ZnFe_2O_4$ nanocrystals are 54.2, 63.5, 100.5 m^2/g, respectively, with the decrease of crystallite size. Therefore it is likely that due to their suitable band gap from the UV-light response discussed above and high specific surface area, the as-synthesized $ZnFe_2O_4$ nanocrystals produce large amounts of electron/hole pairs under UV irradiation with proper wavelength, and thus may show good photocatalytic performance. $ZnFe_2O_4$ sample with 5 $m^2\ g^{-1}$ of specific surface area prepared by the conventional solid-state method at 1000 °C for 12 h is used here as a reference sample, making direct comparison of the catalytic activity of the two kinds of zinc ferrite materials possible.

Temporal evolution of the spectral changes taking place during the photo-degradation of AO-II azodye molecule mediated by 9 nm $ZnFe_2O_4$ nanocrystal is displayed in Fig. 12. As expected, a gradual decrease in the intensity of strong absorption band at 484 nm for AO-II solutions due to the n–π* transitions of azo bond

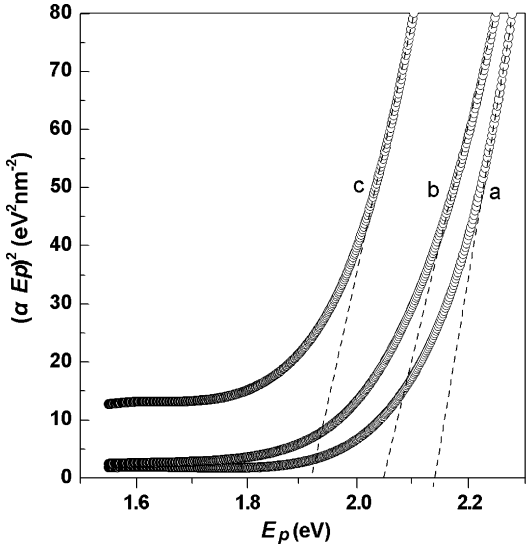

Fig. 11. Tauc plot for $ZnFe_2O_4$ with different crystallite sizes of (a) 9 nm, (b) 14 nm and (c) 19 nm.

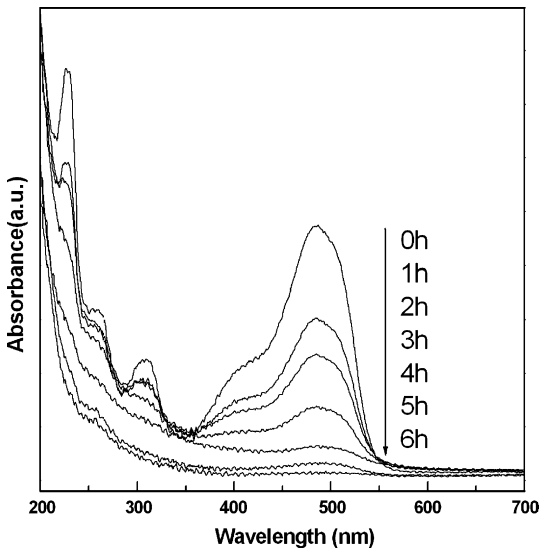

Fig. 12. Absorption changes of AO-II solution during the photo-degradation process over 9 nm $ZnFe_2O_4$ sample under UV-light irradiation.

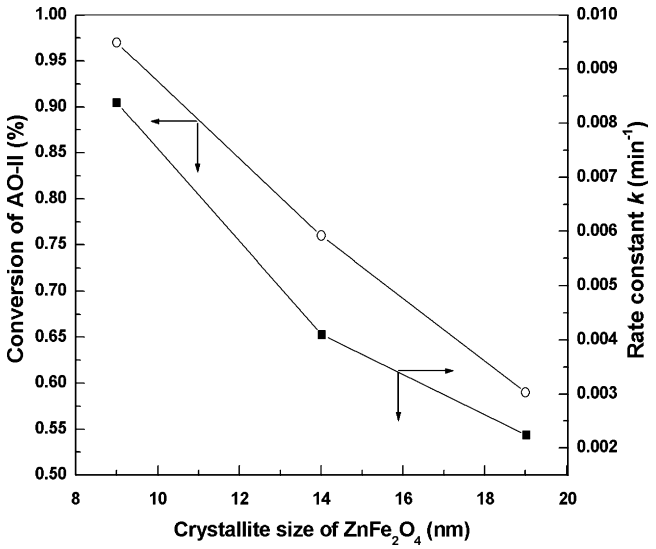

Fig. 14. Influence of the crystallite size of $ZnFe_2O_4$ sample on the degradation percentage of AO-II and kinetic rate constant after 6 h under UV-light irradiation.

is observed during the course of the photoassisted degradation, indicating that the azo groups has been destroyed [40]. Meanwhile, the other absorption at 309 and 230 nm attributed to the π–π^* transition related to aromatic rings decreases significantly along with irradiation time and no new bands appear, implying that full oxidative decomposition had occurred and that other intermediates are no longer formed. The above result indicates that the $ZnFe_2O_4$ nanocrystals indeed exhibit good activity for the photo-degradation of AO-II under UV-light irradiation.

The dependence of AO-II photo-degradation on the crystallite size of $ZnFe_2O_4$ nanocrystals under UV-light irradiation has been investigated at the same operating conditions. As shown in Fig. 13, three $ZnFe_2O_4$ nanocrystals with different crystallite sizes exhibit good photo-degradation activity for AO-II, and there are no obvious degradation of dye molecules was observed in the darkness. It is found that the photocatalytic activity is gradually enhanced with decreasing crystallite size. Especially, the degradation percentage of AO-II after 6 h on 9 nm $ZnFe_2O_4$ sample was as high as 97%.

The dependence of AO-II photo-degradation on the crystallite size of $ZnFe_2O_4$ nanocrystals can be figured out more clearly from Fig. 14, illustrating that the degradation percentage of AO-II and kinetic rate constant k (first-order) basing on the Langmuir–Hinshelwood model increase obviously with the crystallite size of $ZnFe_2O_4$ nanocrystals. Firstly, it is mainly because the generated conduction band of nanosized $ZnFe_2O_4$ semiconductor with the larger optical band gap is more negative and the valence band is more positive, which makes the oxidation and reduction abilities of photogenerated holes increasing [8,41]. Secondly, the smaller size can lead to a shorter time for the electron diffusion from bulk phase to interface, hence decreases the probability of holes coupling with electrons [42,43]. Finally, the higher surface areas also facilitates to the absorption of dye molecules on the surfaces of $ZnFe_2O_4$, which makes the free radical more chance to touch with dye molecules thus giving a faster reaction speed. On the other hand, it should be noted that all $ZnFe_2O_4$ samples prepared by modified reduction–oxidation route show higher conversion of AO-II dye during the course of photo-degradation, as compared to bulk $ZnFe_2O_4$ sample prepared by the conventional solid-state method, due to the large particle size and low surface area of bulk $ZnFe_2O_4$ sample. In addition, as discussed above, as-synthesized $ZnFe_2O_4$ nanocrystals can be excited under visible light, which expands their utilization scope. Further work on the visible-light derived photocatalytic properties of nanocrystalline $ZnFe_2O_4$ materials is currently underway in our laboratory.

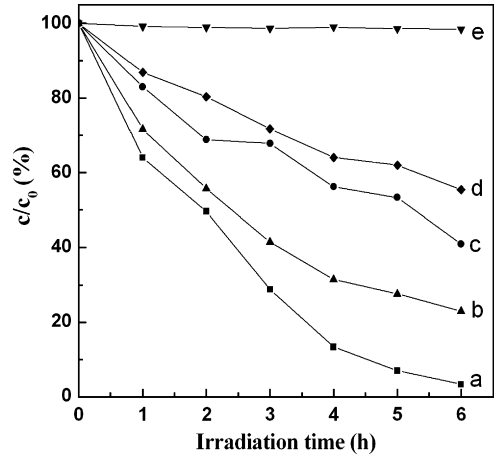

Fig. 13. Photo-degradation of AO-II monitored as the normalized concentration change vs irradiation time using series samples under UV-light irradiation: (a) 9 nm $ZnFe_2O_4$, (b) 14 nm $ZnFe_2O_4$, (c) 19 nm $ZnFe_2O_4$, (d) bulk $ZnFe_2O_4$ and (e) dark reaction with 9 nm $ZnFe_2O_4$.

4. Conclusions

Zinc ferrite nanocrystals with the average crystallite sizes of 9, 14 and 19 nm were successfully prepared by a modified reduction–oxidation method, which involves a very rapid mixing of ferric cations with reducing agent and nucleation of metallic iron by reduction within a very short time in a colloid mill reactor, followed by slow oxidation of iron and structural transformation under hydrothermal conditions. It is believed that the extreme forces, to which the nucleation of metallic iron obtained with a very short time was subjected in the colloid mill, prevented aggregation of the newly formed iron nuclei. Consequently, when the resulting iron nuclei were slowly oxidized in a Zn^{2+}-containing aqueous solution under separate hydrothermal treatment, well-crystallized $ZnFe_2O_4$ nanocrystals with narrow size distribution were obtained. Meanwhile, the photo-degradation investigation reveals that as-synthesized $ZnFe_2O_4$ nanocrystals displayed good abilities to photodecompose acid orange II under UV irradiation,

and that the reduced crystallite sizes of $ZnFe_2O_4$ nanocrystals can lead to an enhanced photocatalytic activity, proceeding from the quantum confinement effect and high specific surface area structure. The findings in this work are believed to provide further insights to understanding of relation between the structure of $ZnFe_2O_4$ nanocrystals and their photocatalytic properties, which is significantly crucial to generate the desired photocatalyst. It can be expected that as-synthesized zinc ferrite nanocrystals with excellent structural properties, such as high thermal stability and strong resistance to acid and alkali, may have potential applications in the field of industrial photo-degradation of organic azodye pollutants.

Acknowledgements

We gratefully thank the financial support from the National Natural Science Foundation of China, 973 Program (2009CB939802), 111 Project (No. B07004) and Changjiang Scholars and Innovative Research Team in Universities (IRT 0406).

References

[1] P. Boldrin, A.K. Hebb, A.A. Chaudhry, L. Otley, B. Thiebaut, P. Bishop, J. Darr, Ind. Eng. Chem. Res. 46 (2007) 4830–4838.
[2] H.H. Hamdeh, Z. Xia, R. Foehrweiser, B.J. McCormick, R.J. Willey, G. Busca, J. Appl. Phys. 76 (1994) 1135–1140.
[3] W.Z. Xiong, G.M. Kale, Anal. Chem. 79 (2007) 3561–3567.
[4] H. Deng, X.L. Li, Q. Peng, X. Wang, J.P. Chen, Y.D. Li, Angew. Chem. Int. Ed. 44 (2005) 2782–2785.
[5] C.W. Yao, Q.S. Zeng, G.F. Goya, T. Torres, J.F. Liu, H.P. Wu, M.Y. Ge, Y.W. Zeng, Y.W. Wang, J.Z. Jiang, J. Phys. Chem. C 111 (2007) 12274–12278.
[6] J.J. Liu, G.X. Lu, H.L. He, H. Tan, T. Xu, K. Xu, Mater. Res. Bull. 31 (1996) 1049–1056.
[7] J.A. Toledo-Antonio, N. Nava, M. Martínez, X. Bokhimi, Appl. Catal. A 234 (2002) 137–144.
[8] J. Qiu, C. Wang, M. Gu, Mater. Sci. Eng. B 112 (2004) 1–4.
[9] Z.H. Yuan, L.D. Zhang, J. Mater. Chem. 11 (2001) 1265–1268.
[10] M. Kobayashi, H. Shirai, M. Nunokawa, Ind. Eng. Chem. Res. 41 (2002) 2903–2909.
[11] M. Tsukada, K. Abe, Y. Yonemochi, A. Ameyama, H. Kamiya, S. Kambara, H. Moritomi, T. Uehara, Powder Technol. 180 (2008) 232–238.
[12] M. Sivakumar, T. Takami, H. Ikuta, A. Towata, K. Yasui, T. Tuziuti, T. Kozuka, D. Bhattacharya, Y. Iida, J. Phys. Chem. B 110 (2006) 15234–15243.
[13] M. Atif, S.K. Hasanain, M. Nadeem, Solid State Commun. 138 (2006) 416–421.
[14] J.M. Yang, F.S. Yen, J. Alloys Compd. 450 (2008) 387–394.
[15] J.A. Zhao, L.W. Mi, H.W. Hou, X.J. Shi, Y.T. Fan, Mater. Lett. 61 (2007) 4196–4198.
[16] H.M. Widatallah, I.A. Al-Omari, F. Sives, M.B. Sturla, S.J. Stewart, J. Magn. Magn. Mater. 320 (2008) 324–326.
[17] M. Jean, V. Nachbaur, J. Alloys Compd. 454 (2008) 432–436.
[18] H. Xue, Z.H. Li, X.X. Wang, X.Z. Fu, Mater. Lett. 61 (2007) 347–350.
[19] R.D.K. Misra, S. Gubbala, A. Kale, W.F. Egelhoff-Jr, Mater. Sci. Eng. B 111 (2004) 164–174.
[20] M.A. Gabal, A.A. El-Bellihi, H.H. El-Bahnasawy, Mater. Chem. Phys. 81 (2003) 174–182.
[21] A. Kundu, S. Anand, H.C. Verma, Powder Technol. 132 (2003) 131–136.
[22] M. Mouallem-Bahout, S. Bertrand, O. Peña, J. Solid State Chem. 178 (2005) 1080–1086.
[23] Z. Gu, X. Xiang, G. Fan, F. Li, J. Phys. Chem. C 112 (2008) 18459–18466.
[24] M.R. Hoffmann, S.C. Martin, W. Choi, D.W. Bahnemann, Chem. Rev. 95 (1995) 69–96.
[25] S. Thimmaiah, M. Rajamathi, N. Singh, P. Bera, F. Meldrum, N. Chandrasekhar, R. Seshadri, J. Mater. Chem. 11 (2001) 3215–3221.
[26] L. Wang, Y. Yu, P.C. Chen, D.W. Zhang, C.H. Chen, J. Power Sources 183 (2008) 717–723.
[27] N.C. Halder, C.N. Wagner, Adv. X-Ray Anal. 9 (1966) 91–102.
[28] Y. Zhao, F. Li, R. Zhang, D.G. Evans, X. Duan, Chem. Mater. 14 (2002) 4286–4291.
[29] G.X. Tong, J.G. Guan, Z.D. Xiao, F.Z. Mou, W. Wang, G.Q. Yan, Chem. Mater. 20 (2008) 3535–3539.
[30] D. Zhao, X. Wu, H. Guan, E. Han, J. Supercrit. Fluids 42 (2007) 226–233.
[31] F.A. López, A. López-Delgado, J.L. Martín-de-Vidales, E. Vila, J. Alloys Compd. 265 (1998) 291–296.
[32] F.S. Lia, L. Wang, J.B. Wang, Q.G. Zhou, X.Z. Zhou, H.P. Kunkel, G. Williams, J. Magn. Magn. Mater. 268 (2004) 332–339.
[33] Y.J. Tang, Y.M. Li, J. Song, Z.D. Pan, Acta Phys. Chim. Sin. 23 (2007) 717–722.
[34] G.C. Allen, K.R. Hallam, Appl. Surf. Sci. 93 (1996) 25–30.
[35] T. Yamashita, P. Hayes, Appl. Surf. Sci. 254 (2008) 2441–2449.
[36] Q. Li, R.C. Xie, Y.W. Li, E.A. Mintz, J.K. Shang, Environ. Sci. Technol. 41 (2007) 5050–5056.
[37] P.S. Patil, L.D. Kadam, C.D. Lokhande, Thin Solid Films 272 (1996) 29–32.
[38] C.H.B. Ng, W.Y. Fan, J. Phys. Chem. B 110 (2006) 20801–20807.
[39] B. Liu, H.C. Zeng, J. Phys. Chem. B 108 (2004) 5867–5874.
[40] L.C. Abbott, S.N. Batchelor, J. Oakes, B.C. Gilbert, A.C. Whitwood, J.R.L. Smith, J.N. Moore, J. Phys. Chem. A 109 (2005) 2894–2905.
[41] R.R. Yeredla, H.F. Xu, J. Phys. Chem. C 112 (2008) 532–539.
[42] J.G. Yu, J.C. Yu, W.K. Ho, M.K.-P. Leung, B. Cheng, G.K. Zhang, X.J. Zhao, Appl. Catal. A 255 (2003) 309–320.
[43] J.C. Yu, J.G. Yu, J.C. Zhao, Appl. Catal. B 36 (2002) 31–43.